Journal of the European Ceramic Society 35 (2015) 4203–4209

Contents lists available at www.sciencedirect.com

Journal of the European Ceramic Society

journal homepage: www.elsevier.com/locate/jeurceramsoc

High-temperature compressive creep behaviour of perovskite-type oxides $SrTi_{1-x}Fe_xO_{3-\delta}$

S.F.P. ten Donkelaar[a], V. Stournari[b], J. Malzbender[b,*], A. Nijmeijer[a], H.J.M. Bouwmeester[a,*]

[a] University of Twente, Faculty of Science and Technology, Inorganic Membranes, MESA+ Institute for Nanotechnology, Enschede, The Netherlands
[b] Forschungszentrum Jülich GmbH, Institute of Energy and Climate Research-IEK-2, Leo- Brandt-Str. 1, D-52425 Jülich, Germany

ARTICLE INFO

Article history:
Received 5 June 2015
Received in revised form 28 July 2015
Accepted 1 August 2015
Available online 14 August 2015

Keywords:
Compressive creep
Perovskite
$SrTi_{1-x}Fe_xO_{3-\delta}$ (STF)
Oxygen transport membrane (OTM)

ABSTRACT

Compressive creep tests have been performed on mixed ionic-electronic conducting perovskite-type oxides $SrTi_{1-x}Fe_xO_{3-\delta}$ (STF, $x = 0.3$, 0.5 and 0.7). Observed activation energies and stress exponents, at 800–1000 °C and in the stress range 10 100 MPa, indicate that the steady-state creep rate of STF under these conditions is predominantly limited by cation lattice diffusion (Nabarro-Herring creep). The effective stress exponents reflect a contribution of dislocation creep to the mechanism of creep in STF30 ($x = 0.3$). The observed creep rates are compared with those exhibited by related perovskite-type oxides, and are discussed in view of the possible application of STF as oxygen transport membrane (OTM).

1. Introduction

Oxygen transport membranes (OTM's) are extensively investigated for their possible integration in oxy-fuel and pre-combustion processes with CO_2 capture [1–3]. In this technology mixed oxygen ionic and electronic conducting membranes are utilized, at elevated temperatures (800–900 °C), to supply oxygen from the pressurized air side of the dense sintered membrane to a fuel, or indirectly to a fuel, or coal via a suitable sweep gas at the opposite side of the membrane. In the latter case, a portion of the CO_2—containing flue gas may be fed back as the sweep gas. Currently, the focus of research activities in the field lies in identifying candidate membrane materials, which combine a high oxygen flux with a high thermochemical stability and durability under oxidizing and reducing conditions, humid and/or CO_2—containing atmospheres.

Recently, we have identified the perovskite oxide $SrTi_{1-x}Fe_xO_{3-\delta}$ (STF) as a promising membrane material [4]. Compositions in this series, especially those with a high iron content, exhibit high values for the ambipolar conductivity [5,6] and oxygen surface exchange kinetics [5,7] that are comparable to those of well-known $La_{0.6}Sr_{0.4}Co_{0.2}Fe_{0.8}O_{3-\delta}$ (LSCF) [8,9], $Sm_{0.5}Sr_{0.5}CoO_{3-\delta}$ (SSC) [10,11], and $La_{0.3}Sr_{0.7}CoO_{3-\delta}$ (LSC) [12] cathode materials for the solid oxide fuel cell (SOFC). STF adopts an ideal cubic perovskite structure (space group Pm−3m), and forms a continuous solid solution between the two end members $SrFeO_{3-\delta}$ and $SrTiO_3$ [13,14]. The structural phase transition to orthorhombic brownmillerite in $SrFeO_{3-\delta}$ below 850 °C [15] is prevented already at a low Ti substitution, $x = 0.01$ [16]. Functional properties, such as the chemical and mechanical stability, thermal expansion and oxygen flux can be tailored by varying the compositional parameter x in $SrTi_{1-x}Fe_xO_{3-\delta}$.

Amongst others, creep is a key factor influencing the operational reliability of OTM membranes [17,18]. Creep is known to be more severe in high-temperature environments, and in systems that continuously endure stress gradients [19]. Stress gradients in the OTM membrane operating at high temperatures are inherent to its operation, and are created mainly by chemical potential gradients and the trans-membrane pressure differential. For long term service the creep deformation should not exceed 1% strain per year [20]. In the present work, the compressive creep behaviour of different STF compositions is investigated as a function of stress and temperature.

2. Experimental

$SrTi_{1-x}Fe_xO_{3-\delta}$ powders with $x = 0.3$, 0.5 and 0.7 (referred to as STF30, STF50 and STF70, respectively) were synthesized by spray pyrolysis (NTNU, Norway) in a continuous air flow at 860 °C, using precursor solutions containing stoichiometric amounts of cations. The obtained raw powders were calcined at 950 °C for 12 h in stag-

---

* Corresponding authors.
E-mail addresses: j.malzbender@fz-juelich.de (J. Malzbender), h.j.m.bouwmeester@utwente.nl (H.J.M. Bouwmeester).

http://dx.doi.org/10.1016/j.jeurceramsoc.2015.08.002
0955-2219/

nant air and ball-milled in ethanol for 24 h. The phase purity was checked using X-ray powder diffraction (D2 PHASER, Bruker AXS, Germany) with Cu Kα. A continuous scan mode was used to collect 2θ data in the range 20–90° with a step size of 0.0202° and counting time of 1 s/step. Powders were uniaxially pressed at 50 MPa followed by isostatic pressing at 400 MPa to rectangular bars with a relative green density of about 60%. These bars were subsequently sintered in the range 1180–1300 °C for 20 h under stagnant air, using heating and cooling rates of 0.5 °C min^{-1}, to a relative density in excess of 95%.

For creep tests, sintered bars were machined to average dimensions ~4 × 5 × 12 mm^3. The ~4 × 5 mm^2 end faces of the samples were parallelized by grinding and finally polished for 1 h using 1 μm diamond paste in order to minimize surface effects and superimposed bending by misalignments. Creep-tested samples showed no sign of barrelling, buckling or formation of cracks. Compressive creep test were performed in ambient air under a constant uniaxial load, corresponding to nominal stresses in the range 10–100 MPa, using an electromechanical testing machine (Instron 1362) equipped with a high temperature furnace. The samples were mounted between two alumina push rods. A linear variable differential transformer (LVDT, Sangami) was used for measurement of the vertical displacement in a range ±1 mm and with a precision of 1.25 μm. The load was controlled with a 10 kN load cell (Interface 1210 ACK), while the temperature was monitored with a K-type thermocouple located near the sample surface. Creep measurements were conducted, in air, from 800 to 1000 °C. The temperature was incremented step wise with 50 °C intervals, using heating and cooling rates of 0.5 °C min^{-1}. For STF50, measurements were also conducted after evacuating the sample chamber to an oxygen partial pressure (pO_2) of ~4 × 10^{-5} bar. Additional details of the creep testing procedure are described elsewhere [21,22].

Creep parameters were obtained by fitting the experimental data of the steady-state creep rate, $\dot{\epsilon}$, to the generalized power law relationship [19],

$$\dot{\epsilon} = A\left(\frac{1}{d}\right)^{p}\sigma^{n}\exp(-\frac{E_a}{RT}) \qquad (1)$$

where A is a proportionality parameter, d the grain size, p the inverse grain size exponent, σ the applied stress, n the stress exponent, E_a the apparent activation energy, R the universal gas constant and T the temperature. The value for n, at given temperature, was calculated from the slope of the log–log plot of $\dot{\epsilon}$ versus σ (Norton plot). The value for E_a, at constant stress, was calculated from the slope of the Arrhenius plot of $\dot{\epsilon}$.

X-ray diffraction patterns (XRD, D4 ENDEAVOR, Bruker AXS, Germany) of the ceramics were recorded before and after creep experiments using Cu-Kα radiation. A continuous scan mode was used to collect XRD data in the 2θ range 10–130° with a step size of 0.01° and a counting time of 5 s/step. Microstructural characterization of the samples before and after creep experiments was carried using scanning electron microscopy (SEM) and electron backscatter diffraction (EBSD). SEM and EBSD patterns were obtained on a Carl Zeiss Merlin© fitted with the Oxford Instruments' Nordlys II EBSD detector with AZtec© 2.4 software. Longitudinal cross-sections were cut from the central part of the samples. For the creep-tested specimens these correspond to the direction parallel to the loading direction. The sample cross-sections were mechanically polished using 0.25 μm diamond paste, and slightly etched with colloidal SiO$_2$. Pt coatings were applied by sputtering. SEM images and EBSD patterns were generated using an accelerating voltage of 20 kV and a beam current of 2 nA. The grain orientation was mapped with a spatial resolution of 0.1477 μm and an angular resolution of ~1°. Data was acquired at 70° tilted samples. Grain size and orientation maps were produced using the HKL Channel 5 Tango software. The AnalysisPro© software package was used for estimation of the grain size. Since the linear intercept and equivalent circular diameter (ECD) methods revealed good agreement in initial tests, the more simple ECD method was used in subsequent analyses.

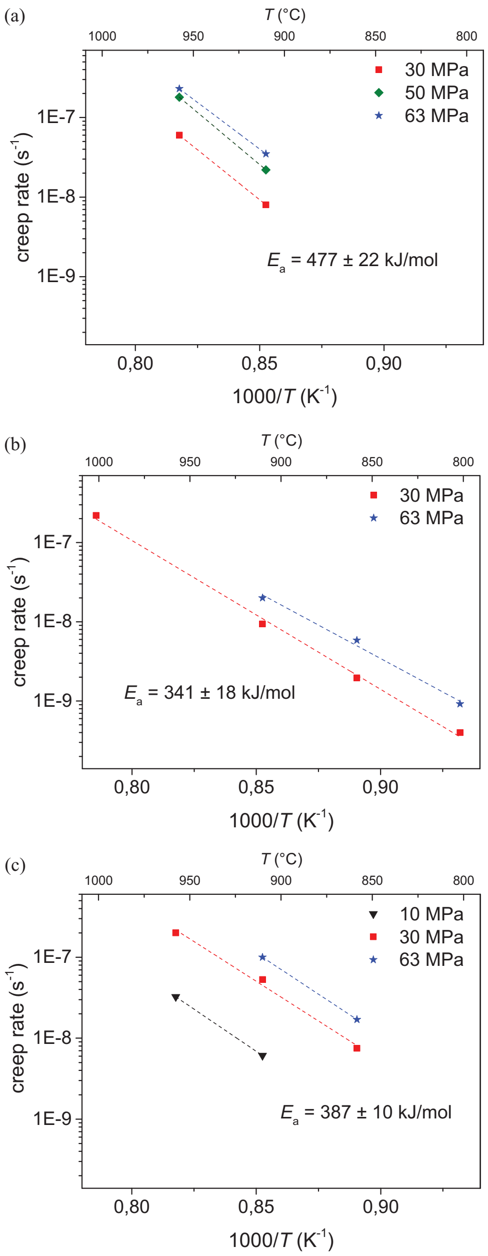

Fig. 1. Temperature dependence of the steady-state creep rate for (a) STF30, (b) STF50, and (c) STF70 tested in air at different stresses.

3. Results and discussion

3.1. Creep measurements

Fig. 1 shows Arrhenius plots of the steady-state creep rate of STF ceramics in air at different stress values. Apparent activation energies, E_a, averaged over the values obtained from measurements at different stresses are in the range 341–477 kJ mol^{-1}. The stress exponents n extracted from the Norton plots (Fig. 2) vary between 1.1 and 2.4. Values of E_a and n obtained for the different STF compositions are listed in Table 1. Hysteresis effects of the creep rate upon thermal cycling were small and found to be within experimental

Table 1
Stress exponents and average apparent activation energies from steady-state creep measurements under air in the stress range 30–63 MPa. The ± values denote standard deviations.

x	E_a (kJ/mol)	n(850 °C) (–)	n(900 °C) (–)	n(950 °C) (–)
0.3	477 ± 22	2.0 ± 0.1	2.0 ± 0.1	2.4 ± 0.2
0.5	341 ± 18	1.5	1.2 ± 0.1	–
0.7	387 ± 10	1.2 ± 0.2	1.5 ± 0.1	1.1 ± 0.2

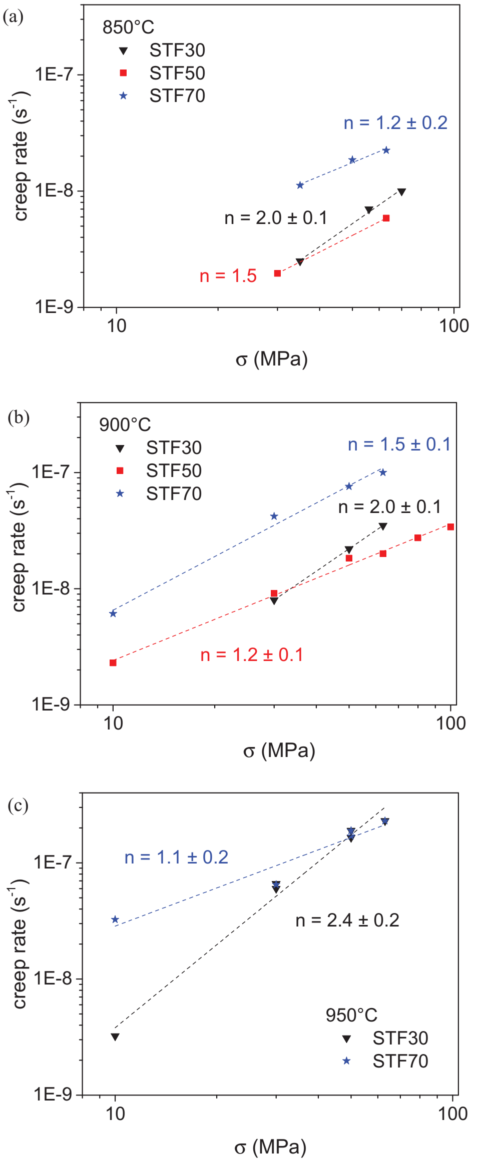

Fig. 2. Stress dependence of the steady-state creep rate for (a) STF30, (b) STF50, and (c) STF70 tested in air at different temperatures.

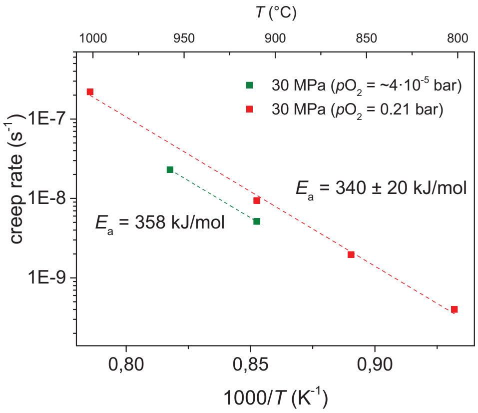

Fig. 3. Temperature dependence of the steady-state creep rate of STF50 at different oxygen partial pressures.

Table 2
Lattice parameters of STF. Data from Steinsvik et al. [13] are shown for comparison. The ± values denote standard deviations.

x	a (this study) (Å)	a [13] (Å)
0.2	–	3.906 ± 0.001
0.3	3.906 ± 0.001	–
0.4	–	3.900 ± 0.001
0.5	3.896 ± 0.001	3.896 ± 0.001
0.6	–	3.890 ± 0.001
0.7	3.888 ± 0.001	–
0.8	–	3.878 ± 0.001

error. Fig. 3 compares the steady-state creep rate of STF50 at two different oxygen partial pressures. The slightly reduced creep rate at the lower pO_2 of ~4 × 10^{-5} bar relative to the value measured at 0.21 bar indicates a role of the oxygen nonstoichiometry of the oxide. Possible mechanisms for creep of STF are discussed below.

3.2. Structure and microstructure analysis before and after creep testing

With the aid of X-ray analysis, the crystalline structure of the ceramic samples was investigated before and after the creep tests. Fig. 4 compares the room temperature XRD patterns of virgin and tested STF compositions. All peaks can be indexed using a cubic perovskite structure (space group $Pm\bar{3}m$). For STF50, these are consistent with PDF 01-084-1004. In none of the samples evidence is found for second phase formation during the creep tests. Lattice parameters obtained from X-ray analysis for each of the compositions before and after creep testing agreed within experimental error. Though the exact oxygen non-stoichiometries of the samples which were cooled in air are not known, Table 2 demonstrates excellent agreement of the lattice parameters with those reported in literature [13].

SEM micrographs and 3D EBSD grain orientation mapping of the samples before and after creep tests revealed a homogenous microstructure. Typical results are shown in Fig. 5. No quantifiable evidence of grain growth during the time span of the creep tests, or a preferred crystallographic orientation of the grains neither before nor after the creep tests was found. The crystal orientation map in the normal (z) direction (Fig. 5c), coloured according to the inverse pole figure scheme (Fig. 5d), indicates that there are no dominant colours. Similar results were obtained in the rolling (y) and transverse (z) directions, and are therefore not shown. Average grain sizes and porosities of the samples from EBSD analyses are compiled in Table 3.

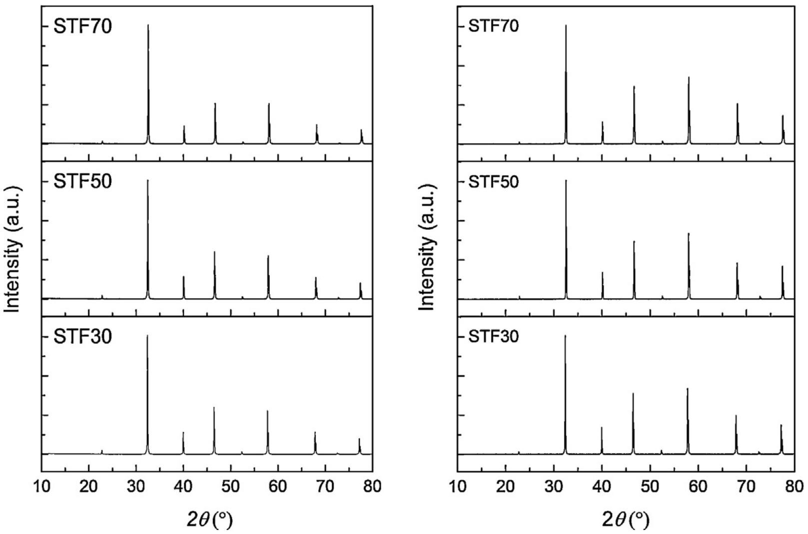

Fig. 4. XRD patterns of STF samples (a) before and (b) after creep measurements.

Table 3
Porosity and grain size of STF samples evaluated 3D EBSD analyses. The ± values denote standard deviations.

x	Porosity (%)	grain size (μm)
0.3	8 ± 1	2 ± 1
0.5	2 ± 1	4 ± 1
0.7	2 ± 1	4 ± 2

3.3. *Creep mechanism*

Diffusion creep involves movement of vacancies via the lattice or along grain boundaries, referred to as Nabarro-Herring and Coble creep, respectively [19]. In diffusion creep, the strain rate is directly proportional to the applied stress, i.e., the stress exponent n equals 1. In the applied stress range 10–100 MPa, the stress exponents for STF50 and STF70 range between 1.1 and 1.5, as can be seen from Table 1. It is thus reasonable to assume that secondary creep in these compositions under the applied experimental conditions is predominantly governed by diffusion of ionic species. Macroscopic strain in a diffusion creep mechanism is known to be inherently accommodated by grain deformation [19]. The significant spread in grain sizes (as reflected by the relatively large standard error in the average grain size (Table 3)), however, did not allow us to quantify grain deformation over the time span of the creep measurements, which would provide an additional premise for diffusion-controlled creep in STF.

For a dislocation creep mechanism, stress exponents n in the range 3–5 are expected [19]. Compared to STF50 and STF70, the derived stress exponents are slightly higher for STF30, varying between 2.0 and 2.4 in the stress range 10–63 MPa covered by the experiments. The latter suggests a partial role of dislocation motion in the creep behaviour of STF30. A power law creep behaviour with stress exponents 1.9–2.5 has also been reported for the related perovskite composition $La_{0.58}Sr_{0.4}Co_{0.2}Fe_{0.8}O_{3\text{-}\delta}$ (LSCF), at 750–900 °C, in the stress range 10–100 MPa [23]. Majkic et al. reported a continuous transition from diffusion to power law creep for $SrCo_{0.8}Fe_{0.2}O_{3\text{-}\delta}$, at 850–975 °C in the stress range 40–80 MPa [24], and for $La_{0.2}Sr_{0.8}Fe_{0.8}Cr_{0.2}O_{3\text{-}\delta}$, at 1100–1200 °C, in the stress range 20–65 MPa [25].

The observed high activation energies for steady-state creep in the STF compositions resemble those measured for cation migration in perovskite oxides as determined from data of diffusion couple and isotope tracer diffusion experiments [26–32]. This observation gives additional support for a diffusion creep mechanism in STF, and excludes oxygen vacancies as the rate-controlling species, since the activation energy for oxygen transport in STF ceramics from data of oxygen permeation measurements is reported to be around 90 kJ mol^{-1} [4].

The slight decrease in the creep rate of STF50 at a pO_2 of ~4×10^{-5} bar relative to that measured under air ($pO_2 = 0.21$ bar) can be accounted for by the enhanced oxygen vacancy concentration at the lower oxygen partial pressure. It should be noted that the concentrations of cation and oxygen vacancies in the ABO_3 perovskite lattice are linked to each other via the Schottky disorder reaction. The latter may be formally written as

$$\text{nil} \Leftrightarrow V_A'' + V_B'''' + 3V_O^{\cdot\cdot} \qquad (2)$$

with equilibrium constant

$$K_s = [V_A''][V_B''''][V_O^{\cdot\cdot}]^3 \qquad (3)$$

with the notion that the B-sites in STF have mixed occupancies. There is significant evidence in literature that the cations in A- and B-site sublattices of perovskite oxides have equal mobility, which includes dopant cations, and which suggests a concerted mechanism for their migration in the lattice [26,27,31,32]. The observation that the apparent activation energies of the creep rate of STF solid solutions are intermediate between those observed for end members $SrFeO_3$ (260 ± 24 kJ mol^{-1} [33]) and $SrTiO_3$ (628 ± 24 kJ mol^{-1} [34]) suggests that the values reflect a weighted sum of contributions from the Schottky formation enthalpy and the migration enthalpies of cations and oxygen ions in STF.

3.4. *Comparison with other mixed conducting oxides*

Fig. 6 compares the steady-state creep rate of STF measured at 900 °C under air in a Norton plot with results from creep studies on related perovskite-type oxides. In general, diffusional creep is prevalent at low stresses and small grain sizes [19], but may give rise to different inverse grain size exponents p in Eq. (1). For a diffusional creep mechanism ($n = 1$) with a vacancy flow through the grains $p = 2$, while $p = 3$ when diffusion of vacancies occurs along grain boundaries [19]. In both mechanisms, the grain-boundaries act as ideal sources or sinks for vacancies. If diffusion is controlled by an interfacial reaction $n = 2$ and $p = 1$. For dislocation creep, the creep rate becomes independent of grain size for dislocation creep;

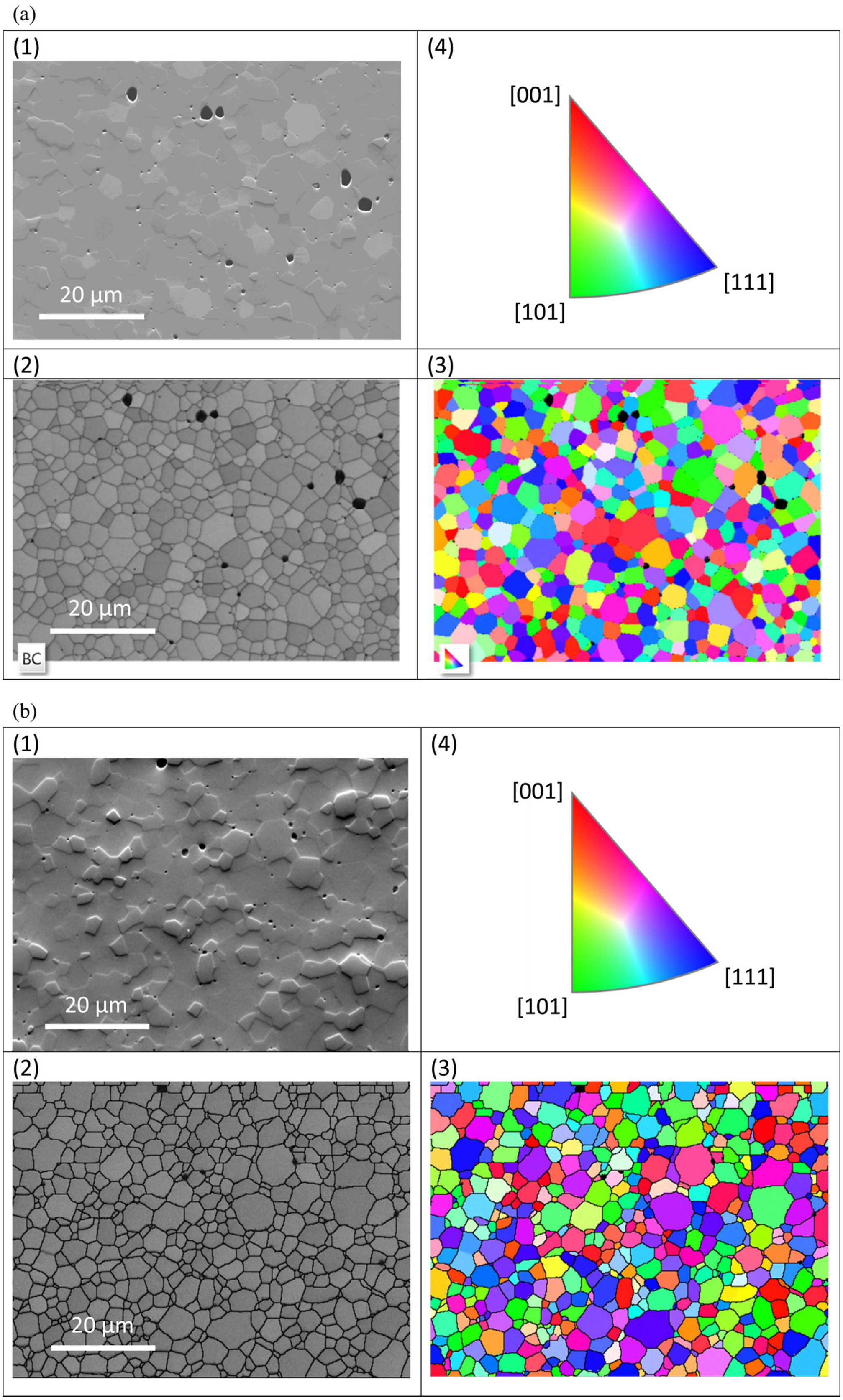

Fig. 5. Microstructure of STF50 (a) before and (b) after creep measurements: (1) SEM fore scatter image, (2) EBSD band contrast image, (3) crystal orientation map (surface normal direction, z) with colour-coding according to the (4) inverse pole figure. In Fig. 5b (2) the grain boundary map is superimposed on the band contrast image.

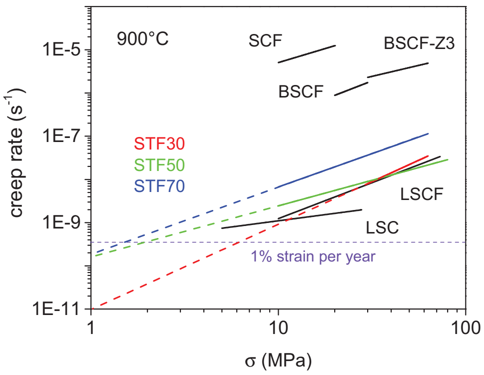

Fig. 6. Comparison of the steady-state creep rates of STF at 900 °C with literature data for related perovskite-type OTM membrane materials: $La_{0.5}Sr_{0.5}CoO_{3-\delta}$ (LSC, 1.2, 1.3, 1.7 µm) [12], $La_{0.6}Sr_{0.4}Co_{0.2}Fe_{0.8}O_{3-\delta}$ (LSCF, 2.2,-, 0.6 µm) [23], $SrCo_{0.8}Fe_{0.2}O_{3-\delta}$ (SCF, 1.4, 1.1, 3.4 µm) [24], $Ba_{0.5}Sr_{0.5}Co_{0.8}Fe_{0.2}O_{3-\delta}$ (BSCF, 1.7, 1.7, 4 µm) [35], and $Ba_{0.5}Sr_{0.5}(Co_{0.8}Fe_{0.2})_{0.97}Zr_{0.03}O_{3-\delta}$ (BSCF-Z3, 1.5,–, 4 µm) [22], where the numbers between brackets indicate the stress exponent, inverse grain-size exponent, and grain size, respectively. Only creep rates lower than 3.2×10^{-10} s^{-1} (indicated by the broken line) are projected to give a creep deformation of less than 1% per year [20].

$n = 3$–5 and $p = 0$ [19]. As the grain size dependence was not measured in this study, the data for STF and other compositions in Fig. 6 are presented 'as measured'.

As seen from Fig. 6, the creep rates of the different STF compositions are intermediate between those of the high-oxygen-flux OTM materials $SrCo_{0.8}Fe_{0.2}O_{3-\delta}$ (SCF) [24] and $Ba_{0.5}Sr_{0.5}Co_{0.8}Fe_{0.2}O_{3-\delta}$ (BSCF) [35] on the one hand, and those of $La_{0.5}Sr_{0.5}CoO_{3-\delta}$ (LSC) [12] and $La_{0.58}Sr_{0.4}Co_{0.2}Fe_{0.8}O_{3-\delta}$ (LSCF) [23] on the other hand. From an engineering design point of view, one of the criteria used in determination of allowable stresses is a 1% creep deformation per year [20], the value of which is presented by the broken line in Fig. 6. As seen from this figure, limiting stress values for the STF compositions, at 900 °C, range between 1 and 7 MPa.

Two main sources contribute to internal stresses in a mixed-conducting ceramic membrane operating under isothermal, steady-state conditions. The first is due to the differential chemical expansion or contraction caused by the gradient in oxygen stoichiometry across its thickness. The chemically induced stresses are reduced when the oxygen flux through the membrane is under partial control by the surface exchange kinetics [36]. Recent stress analysis of supported Zr-doped BSCF (BSCF-Z3) membranes further demonstrate that the stresses induced by oxygen stoichiometry gradients decay with time due to creep [37], leaving only the static trans-membrane pressure differential as the major source of stress in the long term. The mechanical stresses generated by the trans-membrane pressure differential depend on membrane design [37,38]. For a planar membrane, with a trans-membrane pressure differential of 20 bar, the internal stresses may increase to several hundreds of MPa if the membrane support action is concentrated at certain distant points [39]. Significantly lower internal stresses are generated for tubular (or capillary) membrane designs. An additional advantage of the use of tubular membranes over planar membranes is that, as along as tubes' ovality is absent (i.e., for geometrically perfect membranes), tensile stresses can be avoided by operating with an overpressure at the shell side of the membrane [37].

4. Conclusions

The observed activation energies (341–477 kJ mol^{-1}) and stress exponents in the temperature range 800–1000 °C and stress range 10–100 MPa indicate that the steady-state creep rate in STF ceramics under these conditions is predominantly limited by cation lattice diffusion (Nabarro-Herring creep). For STF50 and STF70, the stress exponents are in the range 1.1–1.5. For STF30, however, they are in the range 2.0–2.4, suggesting a contribution of dislocation creep to the creep behaviour of this material. The creep rates of the STF compositions are compared with those exhibited by related mixed conducting perovskite-type oxides considered for use as OTM membrane.

Acknowledgements

The authors gratefully acknowledge financial support for this research from ADEM, A green Deal in Energy Materials of the Ministry of Economic Affairs of The Netherlands (www.adem-innovationlab.nl), and from the Helmholtz Association of German Research Centers (Initiative and Networking Fund) through the MEM-BRAIN Helmholtz Alliance. We further wish to acknowledge Dr. Wessel, Ms. T. Osipova, Mr. R. Küppers and Mr. M. Ziegner for instrumental and technical support, and Dr. G. Pećanac for fruitful discussions.

References

[1] M. Czyperek, P. Zapp, H.J.M. Bouwmeester, M. Modigell, K. Ebert, I. Voigt, W.A. Meulenberg, L. Singheiser, D. Stöver, Gas separation membranes for zero-emission fossil power plants: MEM-BRAIN, J. Membr. Sci. 359 (1–2) (2010) 149–159.

[2] X. Dong, W. Jin, Mixed conducting ceramic membranes for high efficiency power generation with CO_2 capture, Curr. Opin. Chem. Eng. 1 (2) (2012) 163–170.

[3] M.A. Habib, H.M. Badr, S.F. Ahmed, R. Ben-Mansour, K. Mezghani, S. Imashuku, O.G.J. la, Y. Shao-Horn, N.D. Mancini, A. Mitsos, P. Kirchen, A.F. Ghoneim, A review of recent developments in carbon capture utilizing oxy-fuel combustion in conventional and ion transport membrane systems, Int. J. Energ. Res. 35 (9) (2011) 741–764.

[4] F. Schulze-Küppers, S.F.P. ten Donkelaar, S. Baumann, P. Prigorodov, Y.J. Sohn, H.J.M. Bouwmeester, W.A. Meulenberg, O. Guillon, Structural and functional properties of $SrTi_{1-x}Fe_xO_{3-\delta}$ for use as oxygen transport membrane, Sep. Purif. Technol. (2014).

[5] W. Jung, H.L. Tuller, INvestigation of cathode behaviour of model thin-film $SrTi_{1-x}Fe_xO_{3-\delta}$ ($x = 0.35$ and 0.5) mixed ionic-electronic conducting electrodes, J. Electrochem. Soc. 155 (11) (2008) B1194–B1201.

[6] S. Molin, W. Lewandowska-Iwaniak, B. Kusz, M. Gazda, P. Jasinski, Structural and electrical properties of $Sr(Ti{:}Fe)O_{3-\delta}$ materials for SOFC cathodes, J. Electroceram. 28 (1) (2012) 80–87.

[7] C.-Y. Yoo, H.J.M. Bouwmeester, Oxygen surface exchange kinetics of $SrTi_{1-x}Fe_xO_{3-\delta}$ mixed conducting oxides3-, Phys. Chem. Chem. Phys. 11 (2012) 11759–11765.

[8] A. Esquirol, N.P. Brandon, J.A. Kilner, M. Mogensen, Electrochemical characterization of $La_{0.6}Sr_{0.4}Co_{0.2}Fe_{0.8}O_{3-\delta}$ cathodes for intermediate-temperature SOFCs, J. Electrochem. Soc. (2015).

[9] A. Mai, V.A.C. Haanappel, S. Uhlenbruck, F. Tietz, D. Stöver, Ferrite-based perovskites as cathode materials for anode-supported solid oxide fuel cells: part I. variation of composition, Solid State Ionics 176 (15–16) (2005) 1341–1350.

[10] I.C. Fullarton, J.P. Jacobs, H.E. van Benthem, J.A. Kilner, H.H. Brongersma, P.J. Scanlon, B.C.H. Steele, Study of oxygen ion transport in acceptor doped samarium cobalt oxide, Ionics 1 (1) (1995) 51–58.

[11] C. Xia, W. Rauch, F. Chen, M. Liu, $Sm_{0.5}Sr_{0.5}CoO_3$, Solid State Ionics 149 (1–2) (2002) 11–19.

[12] H.L. Lein, K. Wiik, M.A. Einarsrud, T. Grande, E. Lara-Curzio, High-temperature creep behaviour of mixed conducting $La_{0.5}Sr_{0.5}Fe_{1-x}Co_xO_{3-\delta}$ ($0.5 \le x \le 1$) materials, J. Am. Ceram. Soc. 89 (9) (2006) 2895–2898.

[13] S. Steinsvik, R. Bugge, J.O.N. Gjønnes, J. Taftø, T. Norby, The Defect Structure of $SrTi_{1-x}Fe_xO_{3-y}$ ($x = 0$–0.8) investigated by electrical conductivity measurements and electron energy loss spectroscopy (EELS), J. Phys. Chem. Solids 58 (6) (1997) 969–976.

[14] M. Ghaffari, M. Shannon, H. Hui, O.K. Tan, A. Irannejad, Preparation, surface state and band structure studies of $SrTi_{1-x}Fe_xO_{3-\delta}$ ($x = 0$–1) perovskite-type nano structure by X-ray and ultraviolet photoelectron spectroscopy, Surf. Sci. 606 (5–6) (2012) 670–677.

[15] J.-C. Grenier, N. Ea, M. Pouchard, P. Hagenmuller, Structural transitions at high temperature in $Sr_2Fe_2O_5$, J. Solid State Chem. 58 (2) (1985) 243–252.

[16] L.H. Brixner, Preparation and properties of the $SrTi_{1-x}Fe_xO_{3-x/2}/O_{x/2}$ system, Mater. Res. Bull. 3 (4) (1968) 299–308.

[17] M. Lipińska-Chwałek, G. Pećanac, J. Malzbender, Creep behaviour of membrane and substrate materials for oxygen separation units, J. Eur. Ceram. Soc. 33 (10) (2013) 1841–1848.

[18] J. Vente, S. McIntosh, W. Haije, H.J.M. Bouwmeester, Properties and performance of $Ba_xSr_{1\text{-}x}Co_{0.8}Fe_{0.2}O_{3\text{-}\delta}$ materials for oxygen transport membranes, J. Solid State Electrochem. 10 (8) (2006) 581–588.

[19] D.J. Green, An Introduction to the Mechanical Properties of Ceramics. Cambridge Solid State Science Series, Cambridge University Press, 1998, 2015.

[20] L.E. Bool, J.C. Chen, D.R. Thompson, Oxygen Enhanced Combustion for NO_x Control, in Other Information: PBD: 1 Oct 2000. 2000. p. Medium: ED; Size: 9 pages.

[21] B. Rutkowski, J. Malzbender, T. Beck, R.W. Steinbrech, L. Singheiser, Creep behaviour of tubular $Ba_{0.5}Sr_{0.5}Co_{0.8}Fe_{0.2}O_{3\text{-}\delta}$ gas separation membranes, J. Eur. Ceram. Soc. 31 (4) (2011) 493–499.

[22] V. Stournari, S.F.P. ten Donkelaar, J. Malzbender, T. Beck, L. Singheiser, H.J.M. Bouwmeester, Creep behaviour of perovskite-type oxides $Ba_{0.5}Sr_{0.5}(Co_{0.8}Fe_{0.2})_{1\text{-}x}Zr_xO_{3\text{-}\delta}$, J. Eur. Ceram. Soc. 35 (6) (2015) 1841–1845.

[23] B.X. Huang, R.W. Steinbrech, S. Baumann, J. Malzbender, Creep behaviour and its correlation with defect chemistry of $La_{0.58}Sr_{0.4}Co_{0.2}Fe_{0.8}O_{3\text{-}\delta}$, Acta Mater. 60 (6–7) (2012) 2479–2484.

[24] G. Majkic, L. Wheeler, K. Salama, Creep of polycrystalline $SrCo_{0.8}Fe_{0.2}O_{3\text{-}\delta}$, Acta Mater. 48 (8) (2000) 1907–1917.

[25] G. Majkic, L.T. Wheeler, K. Salama, High-temperature deformation of $La_{0.2}Sr_{0.8}Fe_{0.8}Cr_{0.2}O_{3\text{-}\delta}$, Solid State Ionics 146 (3–4) (2002) 393–404.

[26] J. Čermák, I. Stloukal, Collective and Tracer Diffusion via a Defect Cluster in LSGM, Defect. Diffus. Forum 263 (2007) 81–82.

[27] R.A. De Souza, J. Maier, A computational study of cation defects in $LaGaO_3$, PCCP 5 (4) (2003) 740–748.

[28] J.A. Kilner, Ceramic Electrodes for SOFC's, Bol. Soc. Esp. Cerám. Vidrio 37 (2-3) (1998) 247–255.

[29] M. Palcut, K. Wiik, T. Grande, Cation self-diffusion in $LaCoO_3$ and La_2CoO_4 studied by diffusion couple experiments, J. Phys. Chem. B 111 (9) (2007) 2299–2308.

[30] M. Palcut, K. Wiik, T. Grande, Cation self-diffusion and nonstoichiometry of lanthanum manganite studied by diffusion couple measurements, J. Phys. Chem. C 111 (2) (2007) 813–882.

[31] O. Schulz, M. Martin, C. Argirusis, G. Borchardt, Cation tracer diffusion of ^{138}La, ^{84}Sr and ^{25}Mg in polycrystalline $La_{0.9}Sr_{0.1}Ga_{0.9}Mg_{0.1}O_{2.9}$, PCCP 5 (11) (2003) 2308–2313.

[32] H.-I. Yoo, C.-E. Lee, R.A. De Souza, M. Martin, Equal mobility of constituent cations in $BaTiO_3$, Appl. Phys. Lett. 92 (25) (2008) 252103–252103-3.

[33] K. Kleveland, A. Wereszczak, T.P. Kirkland, M.-A. Einarsrud, T. Grande, Compressive creep performance of $SrFeO_3$, J. Am. Ceram. Soc. 84 (8) (2001) 1822–1826.

[34] Z. Wang, S.-I. Karato, K. Fujino, High temperature creep of single crystal strontium titanate ($SrTiO_3$): a contribution to creep systematics in perovskites, Phys. Earth Planet In. 79 (3–4) (1993) 299–312.

[35] J.X. Yi, H.L. Lein, T. Grande, S. Yakovlev, H.J.M. Bouwmeester, High-temperature compressive creep behaviour of the perovskite-type oxide $Ba_{0.5}Sr_{0.5}Co_{0.8}Fe_{0.2}O_{3\text{-}\delta}$, Solid State Ionics 180 (36–39) (2009) 1564–1568.

[36] A. Zolochevsky, A.V. Grabovskiy, L. Parkhomenko, Y.S. Lin, Coupling effects of oxygen surface exchange kinetics and membrane thickness on chemically induced stresses in perovskite-type membranes, Solid State Ionics 212 (0) (2012) 55–65.

[37] K. Kwok, H.L. Frandsen, M. Søgaard, P.V. Hendriksen, Mechanical reliability of geometrically imperfect tubular oxygen transport membranes, J. Membr. Sci. 470 (0) (2014) 80–89.

[38] R. Kriegel, M. Schulz, K. Ritter, L. Kiesel, U. Pippardt, M. Stahn, I. Voigt, Advanced Membrane Design for Oxygen Separation, in ICEPE, Book of Extended Abstracts, Dechema, Frankfurt a.M, 2011, pp. 114–117.

[39] R. Kriegel, Private Communication, Fraunhofer Institute for Ceramic Technologies and Systems (IKTS), Germany, 2015.